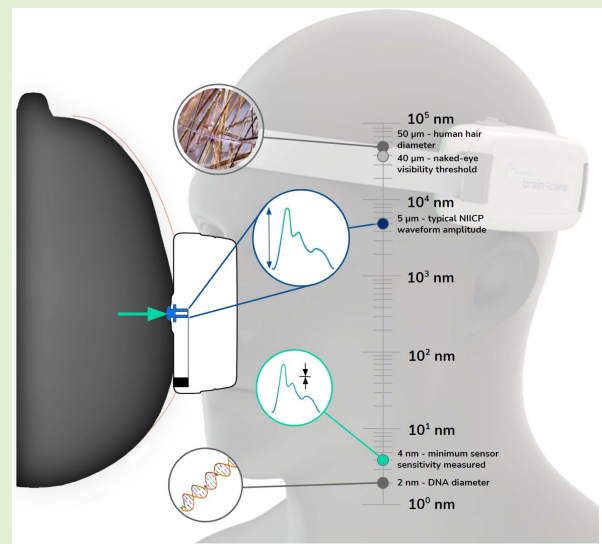


A Nanometer Resolution Wearable Wireless Medical Device for Non Invasive Intracranial Pressure Monitoring

Rodrigo de A. P. Andrade¹, Member, IEEE, Helder Eiki Oshiro¹, Caio Kioshi Miyazaki¹, Cintya Yukie Hayashi¹, Marcos Antonio de Moraes, Rodrigo Brunelli, and João Paulo Carmo¹

Abstract—The non-invasive intracranial pressure (NIICP) method based on a skull deformation has been proven to be a significant tool for an assessment of the intracranial pressure (ICP) and compliance. Herein, we present the development and characterization of a novel wireless sensor that uses this method as its working principle and was designed to be easy to use, to have a high resolution, and to achieve a good accessibility. Initially, a brief review of the physiology fundamentals of the ICP and the historic evolution of the NIICP method are mentioned. The sensor architecture and the rationale for the chosen components are then presented, aiming to ensure nanometer displacement measurements, the conversion of analog resolution to digital at a high speed, the fewest amount of distortion, wireless communication, and signal calibration. The NIICP signal has a typical amplitude of $5\ \mu\text{m}$, and thus a resolution of at least 1% of this amplitude is required for an NIICP waveform analysis. We also demonstrate a 40-nm resolution of the sensor using a nanometric displacement test system that can also respond dynamically for NIICP signals from 50 to 180 bpm without any significant distortion (maximum deviation of P2/P1 ratio of 2.6%). The future applications for this device are broad and can enhance a clinical assessment of the intracranial dynamics.

Index Terms—Non-invasive intracranial pressure, intracranial pressure, intracranial compliance, skull deformation, medical device, wireless sensor, wearable sensor, nanometer resolution, displacement sensor.



I. INTRODUCTION

INNOVATION applied to neurology and neurosurgery advanced in the 1970s with the invention of computed

Manuscript received April 29, 2021; revised June 9, 2021; accepted June 10, 2021. Date of publication June 18, 2021; date of current version October 18, 2021. This work was supported by the brain4care—Braincare Desenvolvimento e Inovação Tecnológica S.A. The work of João Paulo Carmo was supported by Conselho Nacional de Desenvolvimento Científico e Tecnológico (CNPq) under Grant 304312/2020-71. The associate editor coordinating the review of this article and approving it for publication was Dr. Theerawit Wilairasitporn. (Corresponding author: Rodrigo de A. P. Andrade.)

Rodrigo de A. P. Andrade, Helder Eiki Oshiro, Caio Kioshi Miyazaki, Marcos Antonio de Moraes, and Rodrigo Brunelli are with the Engineering Department, Braincare Desenvolvimento e Inovação Tecnológica S.A., São Carlos 13562-420, Brazil (e-mail: rodrigo.andrade@brain4.care; helder.oshiro@brain4.care; caio.miyazaki@brain4.care; marcos.moraes@brain4.care; rodrigo.brunelli@brain4.care).

Cintya Yukie Hayashi is with the Research Department, Braincare Desenvolvimento e Inovação Tecnológica S.A., São Carlos 13562-420, Brazil (e-mail: cintya.hayashi@brain4.care).

João Paulo Carmo is with the Electrical and Computer Engineering Department, University of São Paulo, São Carlos 13566-590, Brazil (e-mail: jcarmo@sc.usp.br).

Digital Object Identifier 10.1109/JSEN.2021.3090648

tomography (CT) scans and magnetic resonance imaging (MRI) [1]–[5]. Many other instruments have been developed since then, incorporating new technologies to medical care, such as catheters for cerebral metabolic analysis [6], stereotactic surgical systems [7], [8], intraoperative neurophysiological monitoring [9], [10], diffuse tensor imaging with fiber tractography [11]–[13], bispectral index [14]–[16], near-infrared spectroscopy monitoring [17], [18], and transcranial Doppler (TCD) ultrasonography [19], [20].

However, these medical specialties always face the challenge of accessing and assessing the intracranial compartment with regard to the Monro-Kellie doctrine [21], [22]. This well-established doctrine considers the dynamic balance between three major components of the central nervous system (CNS): parenchyma–cerebral and spinal cord tissues, arterial and venous blood, and cerebrospinal fluid (CSF). It states that the sum of all component volumes is constant; therefore, any increase in volume of one intracranial component implies a decrease in another to maintain the equilibrium inside the restricted space delimited by the rigid bone structure (skull and vertebral canal), as a compensatory mechanism [21]–[24].

This concept also involves changes in the pressure regimen of this confined compartment, considering any intracranial volume variations that normal physiological mechanisms cannot compensate [24]–[27]. It is presumed, then, that the bone structure is neither compressive nor elastic.

Intracranial pressure (ICP) can be higher than normal in cases of traumatic brain injury, stroke, tumors, hydrocephalus, and other medical conditions [28]–[31]. Intracranial hypertension is often an emergency situation that can cause severe impairments and even death. It requires assertive intervention from healthcare professionals [28], [29], [32], [33]. For this reason, the more information they have on brain functioning, the better the ability to make adequate therapeutic decisions.

Traditional methods of ICP monitoring require surgical intervention or other invasive procedures, such as drilling a hole in the skull to insert a catheter or inserting a needle into the spine [29], [30], [34]. These are considered the gold standard procedures for direct ICP measurements. However, there are some risks associated with them, including direct lesions to the brain tissue, hemorrhages, and infection. Other pitfalls include catheter occlusion or migration and a loss of calibration [30], [34]–[36]. All of these procedures require admission to a healthcare facility, restricting the use of ICP information to certain hospital units and conditions.

In addition, it is not always feasible to use invasive ICP (IICP) monitoring for patients at risk of coagulopathy or other conditions in which the risks of using the invasive device may outweigh the benefits [37]–[39].

Even conventional imaging exams, such as CT scan and MRI, only bring about stationary aspects from inside the cranium and sometimes do not reflect the complex kinetics between components and/or its active tensile compensatory mechanism [40].

In this context, non-invasive methods have been developed to enhance neurological assessments [30]. For instance, ultrasound applied to neuroscience brought about the use of TCD as a portable tool to assess cerebral blood flow (CBF) [20], [41], [42] supplying oxygen and nutrients to the CNS. Another example would be the optic nerve sheath diameter measurement [43], [44], which can indicate an increase in ICP if enlarged. Similarly, the tympanic membrane displacement [30], [45], [46] evaluated by the acoustic reflexes allows insight into ICP as the cochlear fluid pressure, i.e., the fluid of the inner ear is correlated with the CSF pressure.

All of these non-invasive methods monitor ICP indirectly through natural “gaps” provided by the anatomy and also consider the Monro–Kellie doctrine limitation.

By contrast, technological advancements allowed researchers to take a step back and study the bone limitation itself, defying the doctrine [47]. Reviewing basic material physics and engineering concepts, extremely sensitive equipment is able to monitor the expansion of the skull, promoting new strategies to assess intracranial compartment kinetics with less clinical risks for both patients and healthcare professionals. Therefore, we describe here the development of a medical device using a nanometer resolution wireless

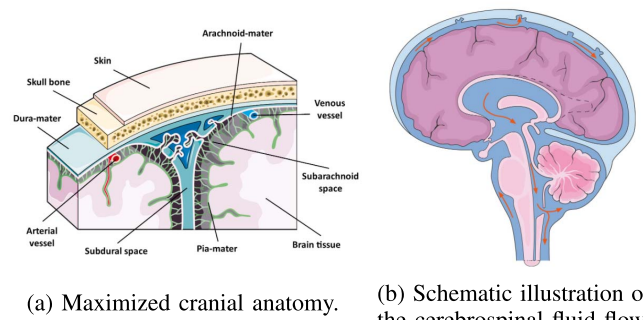


Fig. 1. Simplified anatomical representation of central nervous system [Servier Medical Art, modified].

sensor for non-invasive ICP (NIICP) monitoring based on the principles presented by Oliveira *et al.* [47].

II. INTRACRANIAL PRESSURE

A. Neurophysiology

First, it is necessary to describe the physiological aspects of the CNS, its components (skull, vertebrae, meninges, CSF, parenchyma (brain and spinal cord tissues), blood, arteries, and veins), and the intracranial dynamic that supports the rationale for the development of this new equipment.

The cranium is a bone vault that holds and protects the brain tissue in the same way as the vertebral canal with the spinal cord tissue [24], [48]. The bone structure is supposedly considered inelastic based on the traditional doctrine [21], [22].

The meninges are protective membranes surrounding the core of the CNS (Figure 1a): 1) The dura mater is the thicker layer closest to the internal side of the bone, 2) the arachnoid mater is an intermediate layer with a woven web-like structure, and 3) the pia mater is the most internal and delicate layer that directly covers the brain and spinal cord tissues. The space between the arachnoid mater and the pia mater is called the subarachnoid space and is filled with CSF [27], [48], [49].

The human brain accounts for approximately 2% of the total body weight. Nonetheless, it accounts for 15% of the cardiac blood supply (750–1000 mL) and consumes 20% of the total body oxygen (O₂) metabolism. These numbers show a great energetic demand owing to the neuronal activity requiring a constant blood flow of approximately 45–55 mL per 100 g of nervous tissue per minute [24], [27], [49].

Cerebral vessels have specific anatomical characteristics and physiological properties that can change the diameter instantaneously in response to adverse health conditions, defining cerebral vascular resistance (CVR). Two mechanisms, known as cerebral autoregulation, involve these vascular adjustments to maintain the optimal cerebral perfusion [24], [27], [49]. Cerebral arterioles are able to control the CBF by either dilating when the systemic blood pressure is low or constricting when it is high.

The cerebral venous blood is drained by the venous sinus of the dura mater and superficial and deep veins along the cortex. These veins are unprovided with valves and have larger diameters than the cerebral arteries, contributing to slow blood circulation. Drainage then occurs owing to a negative thoracic cavity pressure, gravity itself, and arterial pulsation [27], [48], [49].

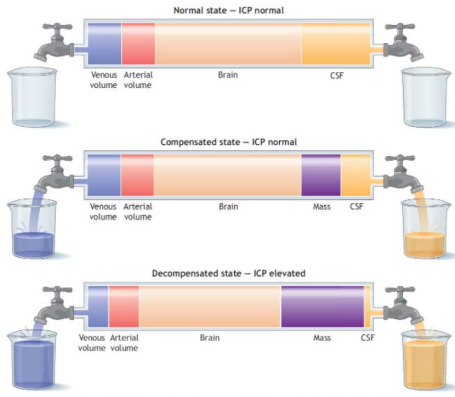


Fig. 2. Compensatory mechanism of ICP [Advanced Trauma Life Support®].

For this reason, cerebral perfusion pressure (CPP) and CVR are key variables in determining the CBF. CPP is calculated as the difference between the mean arterial pressure (MAP) and the cerebral venous pressure (CVP). Basically, it would be the adequate pressure of the incoming blood that guarantees sufficient oxygen and energy supply. There are many difficulties in measuring the CVP, but there is a well-established correlation between the CVP and ICP, the latter being easily measurable [24], [49].

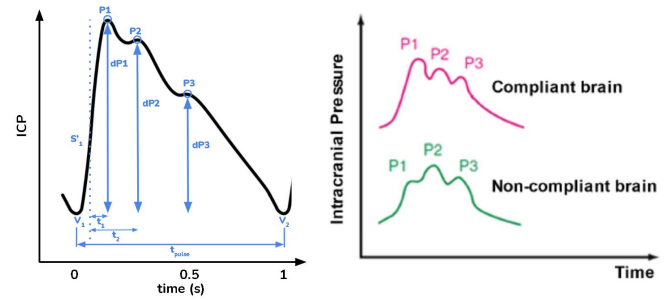
The ICP value can be measured either directly into the cranium with a pressure-sensitive transducer located outside the dura mater (epidural), within the brain tissue (intraparenchymal), and in spaces filled with CSF (intraventricular or subarachnoid), or in the vertebral canal with a manometer connected to a needle if there is a lumbar puncture (subarachnoid space) [49]–[51].

CSF is a clear and homogeneous fluid that is considered an ultrafiltrate of blood plasma. The total amount is estimated to be approximately 140–150 mL. It is secreted by the proliferation of arterioles inside the lateral ventricles, i.e., the choroid plexus. At each cardiac cycle, the blood influx generates small amounts of CSF that spread along the lateral, third, and fourth ventricles, then to the aqueduct of Sylvius and finally to the subarachnoid space down the vertebral canal (Figure 1b). This pulsatile distribution can be translated into a waveform in a similar way to that of the blood pressure waveform [24], [27].

Considering the hydrostatic fundamentals (Pascal's law), the pressure in the leveled interconnected spaces filled with CSF is the same along the neural axis despite the point of measurement. ICP values are commonly registered in mmHg and cmH₂O [24], [27], [49]. Thus, MAP and ICP are normally used to calculate the CPP ($CPP = MAP - ICP$).

Because the parenchyma, CSF, and blood content are confined to the CNS compartment, any mass-effect lesion inside the cranium (e.g., tumor or hematoma) will deploy limited amounts (compensatory reserve) of CSF to the vertebral canal through the subarachnoid space and venous blood content to the thoracic cavity by the jugular vein, owing to their lower resistance, in an attempt to compensate for the intracranial volume and consequently the inner pressure [21]–[24], [52].

Sustained values of above 20 mmHg are considered elevated ICP, and once the compensatory mechanisms reach their



(a) ICP Waveform morphology features extracted from mathematical analysis. (b) Depiction of ICP Waveforms between Compliant and Non-Compliant Brains.

Fig. 3. ICP waveform analysis.

capacity, the pressure gradients inside the cranium can lead to herniations, shifting parts of the brain parenchyma. This dislocation is life-threatening and ends up compressing the vessels, the nerves, and the proximal part of the spinal cord that controls vital functions (brainstem) [51], [53]. The concept of these compensatory limits is related to the exponential intracranial pressure-volume relationship and is commonly referred to as intracranial compliance [54], [55].

B. ICP Waveform Parameters

In addition to the absolute value presented by the ICP monitoring devices, the pulsatile nature of ICP and its derivation from MAP brought to light studies on the pulse waveform characteristics in the same way in which arterial blood pressure is analyzed [56]–[59].

The ICP waveform morphology is a significant tool for evaluating intracranial hypertension and compliance [25], [26], [29], [60], [61]. The ICP pulse waveform, thus far studied using the invasive method, can be characterized based on some of the following items [62]–[66] (Figure 3a):

- Waves: P1 (percussion wave, owing to arterial pressure being transmitted from the choroid plexus to the ventricles), P2 (tidal wave, related to intracranial compliance), and P3 (dicrotic wave, related to the closure of the aortic valve during diastole).
- Amplitude of wave peaks: dP1 (relative amplitude of percussion wave), dP2 (relative amplitude of tidal wave), and dP3 (relative amplitude of dicrotic wave).

Under normal ICP conditions, the amplitudes of these peaks are $P1 > P2 > P3$, and the time elapsed (lag) from the beginning of the pulse waveform until the highest peak is shorter. When compensatory mechanisms are working properly, these peak proportions remain the same, even if there is a volume or pressure change inside the cranium, representing a compliant brain. However, when ICP reaches critical levels or the volume expansion exceeds the compensatory reserve, the pulse waveform morphology changes, disclosing an increase in peak amplitude P2 over P1, and the lag until reaching the highest peak also increases [67], [68] (Figure 3b).

The lag of mechanical propagation of CSF throughout the CNS is also called latency, upstroke time, or time to peak (TTP) in the literature [65], [69]–[73]. To calculate the TTP,

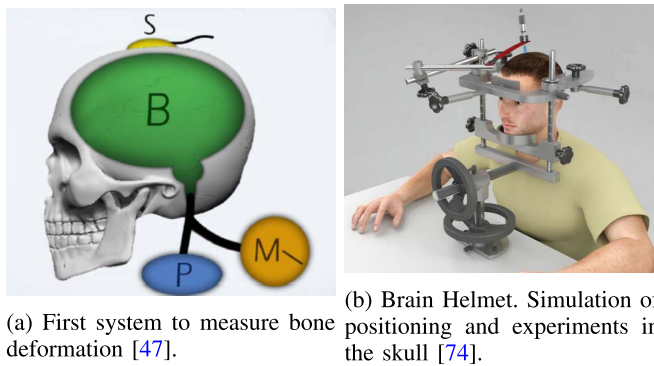


Fig. 4. First experiments involving NIICP method.

the pulse max slope S' is identified (moment in time when the pulse slope is steepest), which is statistically the most stable reference point (technical parameter), and the duration from S' to the highest pulse amplitude is then marked. The normalized TTP, i.e., the relation between the TTP and the total pulse duration, helps interpret when the highest peak of a pulse occurs, independent of the heart rate. If the TTP is longer, the highest peak is likely to be a P2 (ICP tidal wave). However, if the TTP is shorter, it is likely to be a P1 (ICP percussion wave). Figure 3a illustrates these parameters.

Despite the absolute ICP values, healthcare professionals can monitor neurological conditions with waveform morphology information related to intracranial compliance. Unfortunately, there are not many medical devices that can provide such detailed information in an easy way outside clinical research protocols [65], [69]–[73].

Therefore, based on the bedside accessibility challenge, the new comprehension of Monro-Kellie doctrine, and the instigating waveform morphology information, the development of an innovative NIICP monitoring device is described below, including the mechanical method with the hardware and software elements.

III. NON-INVASIVE ICP METHOD - SKULL DEFORMATION

The NIICP method based on the skull deformation is initiated with the proof that the skull is not a non-deformable structure and can be used as a physical parameter for the detection of changes in intracranial volume and pressure, which are governed by a constitutive relation [47].

A. Historic Evolution of the Method

The first experiment conducted using this method was described by Oliveira *et al.* [47], in which a deformation sensor (strain gauges) was applied to the parietal region of a human skull in a laboratory environment, confirming that ICP variations have an almost linear correlation with skull deformation. Figure 4a shows the experimental setup simulating ICP changes by inflating a balloon inside the skull, in which the attached strain gauge sensor was able to measure deformations on the bone surface.

Expanding this hypothesis, a further *in vivo* experiment conducted by Vilela *et al.* [75] validated a minimally invasive ICP monitoring method through a comparison to the standard IICP. In this experiment, strain gauge sensors were

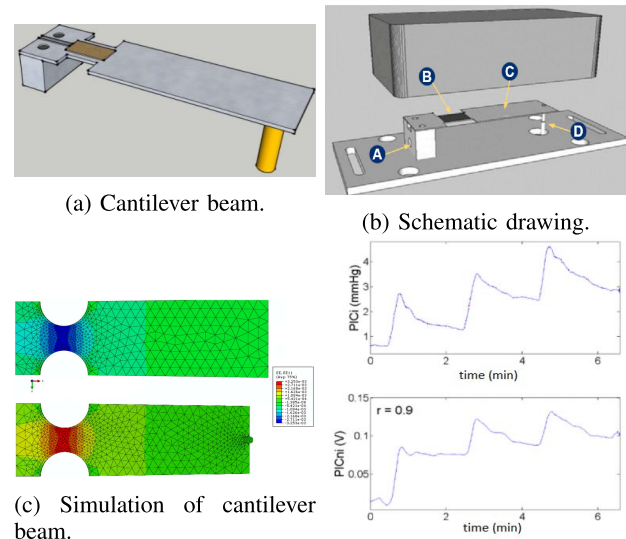


Fig. 5. (a) Cantilever beam with touch pin and strain-gauge. (b) Schematic of main components of non-invasive sensor within the plastic housing: A) support for sensor bar, B) strain gauge sensors, C) sensor cantilever bar, and D) pin. (c) Simulation of stress concentration of cantilever bar. (d) Experiment of three saline infusions in rats.

externally glued onto the exposed skulls of rats, and saline was infused into the vertebral canal to induce changes in the ICP. The skull deformation captured by the strain gauge showed a high positive correlation with the direct IICP values (Pearson's correlation coefficient $r = 0.8 \pm 0.2$, with a range of 0.31–0.99).

Since then, several concepts have been developed to measure this skull deformation in a practical way. Andrade [74] cited a stereotactic apparatus called *Brain Helmet* (Figure 4b) using a cantilever beam, fixed strain gauges, and a pin touching the patient's head to capture the cranial expansion. However, this device has difficulties in keeping the patient's head still. The evolution of these concepts yielded better results when the cantilever beam and strain gauges (Figure 5a) were embedded in a support and an enclosure, enabling the wearable format on a headband (Figure 5b) [74], [76]. In this way, the sensing mechanism used the patient's own head as a relative reference instead of a fixed reference frame like the table used in *Brain Helmet*.

Although the cranial expansion signal was captured by the sensor, each pulse had a high noise-signal ratio. An improvement in the system's signal acquisition and sensor instrumentation by designing a stress concentration in the cantilever beam (Figure 5c) allowed evident amplification of the NIICP signal on the waveform morphology of the animal experiment [74], which is similar to the IICP sensor waveform (Figure 5d).

Frigieri *et al.* [77] used the refined NIICP method in patients with traumatic brain injury. The signal acquisition was possible because the skull deformation is an inherent phenomena that naturally occurs from inside of the cranium, whether the patient is standing up, sitting down or lying down on a resting supine position. They compared the NIICP with the IICP sensors and invasive arterial blood pressure (ABP), and found much more significant similarities between NIICP and IICP

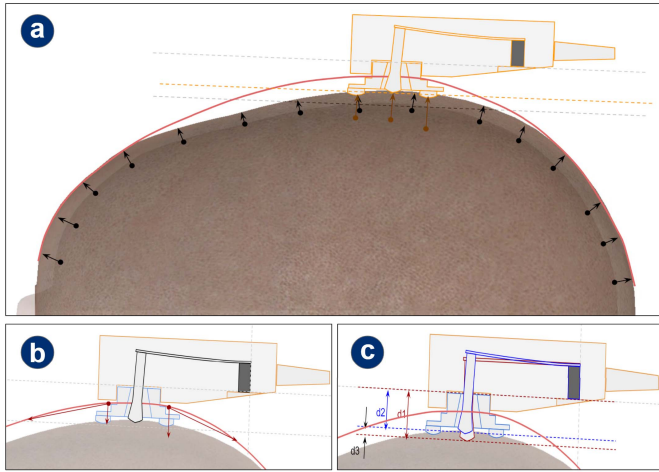


Fig. 6. Sensor working principle: (a) Amplify representation of cranial expansion, (b) headband fixing forces, and (c) displacement transducer of cranial expansion.

than those found between NIICP and ABP. Nevertheless, none of the studies mentioned [74]–[76] were able to establish a direct relationship between NIICP and the absolute values of IICP.

These NIICP studies [74]–[77] presented good evidence that the method is strong in an ICP waveform analysis, allowing the development of a medical device applying a noninvasive assessment of intracranial dynamics and compliance in a commercial manner. The transducer working principle (Subsection III-B) of the first NIICP wired sensor (Model BcSs-PICNI2000, Braincare Desenvolvimento e Inovação Tecnológica S.A., Sao Carlos, Brazil) launched commercially in 2017 was also applied to the current wireless version described below (Model BcSs-PICNIW-1000, Braincare Desenvolvimento e Inovação Tecnológica S.A., Sao Carlos, Brazil).

B. Working Principle

The principle of operation of the sensor is fundamentally based on the studies described in Subsection III-A. The physiological cranial expansion phenomenon starts in the heart, which pumps blood to the brain through arterial vessels. Inside the head, these vessels expand in diameter and cause variations in intracranial volume and pressure. The skull then experiences small deformations owing to these volume and pressure variations (as illustrated in an amplified manner in Figure 6a). By fixing the headband (red line in Figure 6b) with a certain amount of tension, the pin of the sensor touches the head and keeps the device in the lateral area of the head just above the ears (frontotemporal region). The skull deformations can then be perceived as displacements in the pin that bends the cantilever beam of the sensor. Figure 6c illustrates the displacement perceived by the sensor, where the resulting displacement (d_3) is the difference between the initial (d_1) and final (d_2) positions, $d_3 = d_1 - d_2$, fixing the support bar of the sensor as a reference.

When the cantilever beam bends, it causes tension and compression on the fixed strain gauges. The strain gauges in full bridge Wheatstone configuration amplify the mechanical signal and convert it into a proportional electrical signal

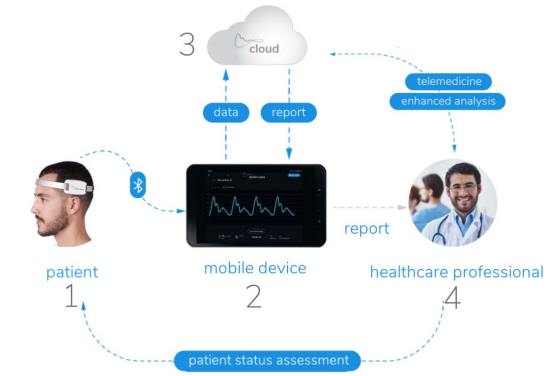


Fig. 7. The brain4care wireless system.

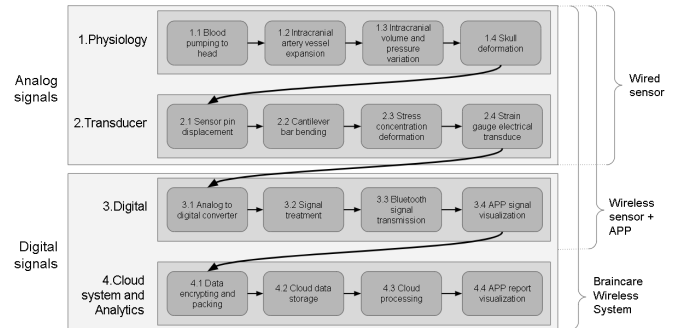


Fig. 8. Signal journey. Block diagram from blood flow to report analysis.

(related to the resistance variation), which is read by an analog signal acquisition system (e.g., multiparameter patient monitor). The working principle is summarized by the block diagram in Figure 8 for groups 1 and 2, where each block is a physical behavior that leads to the next block. Group 1 (physiology group) is a series of biological events that cause a skull deformation, and group 2 (transducer group) is related to how the skull deformation is transduced into an analog electrical signal by the sensor.

C. Motivation

The wired NIICP sensor BcSs-PICNI-2000 demonstrated some limitations, as summarized below, which instigated the functionality enhancement for the new wireless version:

- 1) *Usability*: Moving a patient between sectors in a hospital [78], and even inside a room, is a complex process when a patient is being monitored. The sensors are connected to a multiparameter device that limits the mobility depending on the length of the cables and the bed layout.
- 2) *Monitor compatibility*: The BcSs-PICNI-2000 sensor was developed to be compatible with all patient monitors available on the market that have an invasive pressure input and are in accordance with ANSI AAMI BP22 [79]. However, some models of patient monitors do not display the waveforms with minimum resolution and span necessary for visualization and analysis by health professionals with high quality.
- 3) *Report generation*: To generate reports of a waveform analysis, it is necessary to record the data from the

monitor and then upload them manually for data processing. An integrated and automatic system between the sensor and cloud would make this process easier.

- 4) *Instrumentation sensitivity*: The cantilever beam was designed to be quite thin to sense extremely small variations in the cranial expansion. Unfortunately, some operators overloaded the instrument when handling it during positioning and tightening on the patient's head, causing a plastic deformation in the bar.

IV. WIRELESS SYSTEM, ARCHITECTURE, AND SENSOR DESIGN

The brain4care wireless system (BWS) is derived from the wired system and provides NIICP waveform information for interpretation. This medical device is intended to monitor ICP variations in patients with suspected ICP alterations or changes in intracranial compliance.

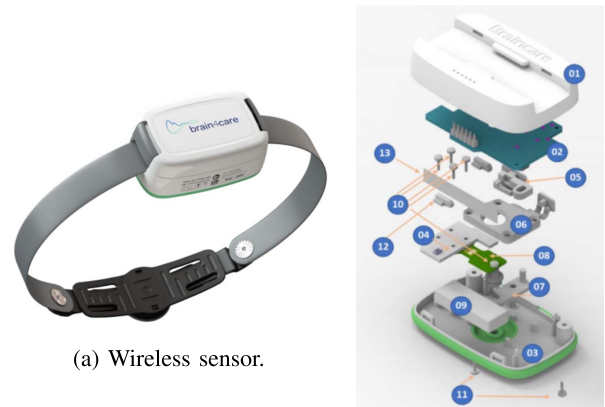
Figure 7 shows the system functionality and overall data journey. The sensor (represented by the number 1 in the figure) contains high-resolution acquisition electronics, and battery powered, it continuously transmits the NIICP signal to a mobile application (mobile app) (2) through a proprietary protocol over a Bluetooth® connection for a clinical assessment in real time. The data are then sent to the cloud (3) through an HTTPS connection on the mobile app. The analytical software inside the cloud includes data parsing, detrending, signal validation, signal filtering, inversion verification, pulse identification, artifact removal, pulse alignment, pulse averaging, and pulse parameter calculation. The processed information is sent back to the mobile app in the form of a report with the waveform image and additional information. There is also the possibility of visualizing the waveform directly on the patient monitor's screen by plugging in a wireless receiver through the invasive pressure input.

The mobile app displays the following information to the healthcare provider (4) for interpretation: a real-time ICP waveform visualized on either the mobile device or the connected multi-parameter patient monitor, preliminary and final reports with an estimated P2/P1 ratio variation through time, an ICP waveform signal over time, a pulse morphology as the average per minute with the P2/P1 ratio, the number of useful pulses, the heart rate (bpm), and the TTP.

In addition to the wired sensor and analog signals described in Section III (groups 1 and 2 of diagram blocks), Figure 8 also includes the BWS implementations and signal journey (groups 3 and 4 of Figure 7). Group 3 starts with the digitization of analog signals (3.1), which leads to signal treatment (3.2) with filtering, error compensation, and voltage to micrometer calibration. The NIICP signal is sent to the APP (3.3), where it can be visualized (3.4). Group 4 involves the cloud and analytics processes of the report generation.

A. Architecture and Design of Brain4care Sensor

The brain4care wireless sensor comprises a mechanical transducer with the same principle as the wired sensor (described in Section III) to capture nanometric skull displacements and embeds a high-resolution and high-speed analog-to-digital converter (ADC).



(a) Wireless sensor.

(b) Sensor exploded view.

Fig. 9. (a) Wireless sensor assembled. (b) 01 - Top sensor housing, 02 - Main PCB, 03 - Bottom sensor housing, 04 - Instrumentation PCB, 05 - ON-OFF Switch, 06 - Mechanism cover, 07 - Contact pin lock, 08 - Cantilever beam, 09 - Internal battery, 10 - Contact pin screw, 11 - Sensor screws, 12 - Sensor travel limiter, 13 - Bluetooth antenna.

B. Displacement Transducer

The displacement transducer was based on a cantilever beam embedded at the bottom of the sensor. The cantilever beam (9b.08) has a rectangular shape with dimensions of approximately 36 mm × 13 mm × 0.38 mm and is made with a beryllium copper alloy that has excellent properties for load cell instrumentation, presenting excellent mechanical properties. There is an isostress concentration that increases the sensitivity that mechanically amplifies up to 3-times the deformation in a homogeneous way over the sensitive region, where double uniaxial strain gauges are glued on each side of the beam to form a full Wheatstone bridge.

C. Hardware e Firmware

Figure 10 shows the hardware functionality of the wireless sensor. Unlike the wired sensor, the wireless sensor sends the waveform signal to mobile devices or receivers on the patient's monitors, and is now responsible for the entire analog front end, analog to digital conversion, compensation of external effects, filters, and electrical signals for displacement calibration.

The analog front end of the NIICP signal is initially composed of a full Wheatstone bridge with compensations of zero, span, and thermal drifts related to cantilever dilation and strain gauge unbalance. The voltage excitation of the bridge was also controlled to ensure the relative reading of the signal. A 32-bit delta-sigma ADC with differential input and a programmable gain amplifier (PGA) is responsible for converting the electrical signal from the sensor, which compensates for the relative signal in $\mu\text{V/V}$. A 24-bit ADC converter is dedicated for reading the sensor temperature for thermal compensation.

Digital filters of the 4th and 5th order are used to guarantee the signal quality against external noises. For this purpose, the system uses two methods to ensure the signal quality against noise. The first is the rotation of the positive and negative pins, in signal reading, to reduce the voltage offset drift, which reduces the noise by a factor of 1.4. The second method is a digital filter, which can be described as

TABLE I
SETAS SPECIFICATIONS

Parameter	Value
Linear Actuator:	
Controller:	
Manufacturer	Physik Instrumente-PI
Model	E-861.1A1 NEXACT
Power supply	24 V, 42 W
Communication	RS-232/USB
Interpolation rate	1000
Encoder read resolution	20 nm
Encoder reading rate	100 S/s
Position writing rate	100 writings/s
Linear Drive:	
Manufacturer	Physik Instrumente-PI
Model	N-310.16 NEXACT
Push/Pull force	10 N
Travel range	125 mm
Open-Loop resolution	1 nm (with E-861)
Operation voltage	-10 to +45 V
Travel range in analog operation	7 μ m
Max. speed	10 mm/s
Scale:	
Manufacturer	Renishaw
Model	RSLM-SS-20U3A-0100-A
Length	130 mm
Readhead	
Manufacturer	Renishaw
Model	T-1011-30A
SDE (typical)	30 nm
Max. speed	10 m/s
Interface:	
Manufacturer	Renishaw
Model	TI0000A00A
Output Type	Two differential sinusoids in quadrature
Period	20 μ m
PXI:	
Manufacturer	National Instruments
Chassi Model	PXIe-1071
PC Controller Model	PXIe-8135
DMM Multimeter Model	PXIe-4081
Bridge Model	PXIe-4330
Multiplex Model	PXI-2527

B. Software

The SETAS software was fully developed in LabVIEW from NI (National Instruments, TX, USA) and designed to both conduct manual readings and prepare routine sets that can be executed automatically.

These routines are structured as tests and subtests that are processed in a predetermined sequence. Each test type has its own execution parameters. The calibration procedure is the main routine standardizing all sensors.

VI. SENSOR CHARACTERIZATION

Experiments were conducted to demonstrate the capability of the wireless sensor, as described in the following characterization sections:

- **Sensor specifications:** technical specifications of the project and performance of the electronics composing the sensor.
- **Sensor precision:** test indicating the stability of the measurements, repeatability, and reproducibility among different sensors within the working range.

TABLE II
WIRELESS SENSOR SPECIFICATIONS

Parameter	Value
Power Consumption Average	45 mA
Internal Battery Autonomy	5 h 50 m
External Battery Autonomy	21 h 30 m
Batteries life	500 cycles (80%)
Dimensions	73.55 mm \times 44.57 mm \times 32.50 mm
NIICP Sample rate	266.1 SPS
ADC ENOB with chop mode enabled	21.38 bits (18.48 free of noise bits)
ADC noise with chop mode enabled	0.099 μ V _{rms} (0.737 μ V _{pp})
Mechanical limit	1500 μ m

TABLE III
FACTORS THAT CONTRIBUTE TO THE VARIABILITY OF THE SIGNAL

Variation factor	Components	Description of measurement
Stability	A	Variability intrinsic to the sensor. It also represents the variability of measurements once the sensor is settled.
Repeatability	B	Variability between repetitions caused by manual handling and positioning a sensor in the test system.
Reproducibility	C	Variability caused only by differences between sensors.
Total variability	A+B+C	Variability considering all factors.

- **Sensor sensitivity:** test indicating the minimum change in input that the sensor can detect
- **NIICP waveform characteristics reproduction:** a comparison between the characteristics of the waveform conducted by SETAS at the sensing pin and the characteristics of the waveform perceived by the sensor.

A. Sensor Specifications

Table II provides a summary of the specifications of the wireless sensor and its main components. The peak-to-peak noise of the ADC (0.737 μ V_{pp}) is equivalent to 51.59 nm when converted into displacement units considering the typical calibration coefficient of 0.35 μ m/ μ V/V and the excitation voltage of 5 V in the instrumentation bridge.

B. Sensor Precision

A stability and precision study involving a total of 33 sensors was conducted to evaluate the factors that contribute to the variability of the measurements, their contribution to sequential measurements, and sequenced repetitions. The variation factors considered are presented and described in Table III.

A total of 33 sensors were tested in this study. A test routine composed of 11 back and forth cycles of 800- μ m displacements (Figure 12a) was repeated three times for each sensor. The first cycle was not computed because of the stabilization. The total number of measurements is shown in Figure 12c.

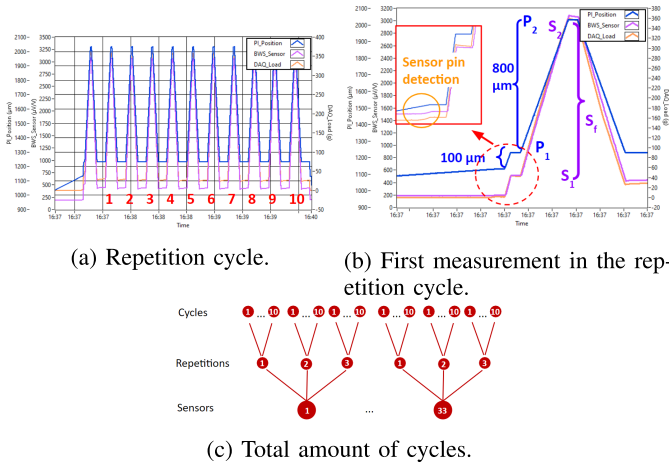


Fig. 12. (a) One repetition round. A total of 990 measurements were taken as illustrated in (c). Item (b) shows in detail the pin detection, initial offset of $100 \mu\text{m}$, and first back and forth cycle of a repetition.

TABLE IV

WIRELESS SENSOR SOURCES OF VARIATION AND CONTRIBUTION

Sources of variation	Variance (μm) ²	Contribution (%)
Stability	3.107	1.11
Repeatability	181.687	64.80
Reproducibility	95.559	34.08
Total variability	280.353	100.00

The signal variation caused by the $800 \mu\text{m}$ variation is calculated as $S_f = S_2 - S_1$, where S_1 and S_2 are the signals in $\mu\text{V/V}$ read by the sensor. This process is illustrated in Figure 12b.

The displacement measured by the sensor is given by $D = (S_2 - S_1) \times (\text{calibration coefficient})$, where the calibration coefficient is the coefficient obtained for each sensor that converts the value obtained from microvolts per volt into micrometers.

The average of the 990 measurements obtained using the wireless sensor was $804.461 \mu\text{m}$. The relation involving the variability factors was modeled using random effects model. The model was solved and the analysis of variance (ANOVA) calculated using **R** programming language and the *lmer* function, contained in the *lme4* package, was used to fit the linear model. Once the variances of each factor and the total variance were calculated, the percentage contribution of each one was obtained.

Table IV lists the variance of each factor and their contribution percentages.

The standard deviations obtained from the variance and their contributions are presented in Table V, followed by the precision limit, calculated as 3 standard deviations (confidence of 99.7% when considering a normal distribution of measurements) and its percentage considering a mean value of $804.461 \mu\text{m}$.

The results indicate that the main contributor to the total variability measured in this test was sensor handling and positioning in the test setup factor (64.08% of the contribution).

TABLE V

WIRELESS SENSOR SOURCES OF VARIATION STANDARD DEVIATION AND CONTRIBUTION, VARIABILITY LIMITS, AND PERCENTAGE DEVIANCE FROM MEAN MEASUREMENT

Sources of variation	Standard deviation (μm)	Total Variation (%)	Precision Limit _{99.7} (μm)	Deviance from mean measurement (%)
Stability	1.763	10.53	5.288	0.66
Repeatability	13.479	80.50	40.437	5.03
Reproducibility	9.775	58.38	29.326	3.65
Total	16.744	100.00	50.232	6.24

The variability in the measurements owing to the differences between sensors was 34.08% of the contribution, and the variability owing to variations intrinsic to a sensor is considerably smaller, with a contribution of 1.11%. In addition, the precision limit among all measurements corresponded to 6.24% of the mean measurement of the range tested ($804 \mu\text{m}$), the main contributor to the deviation was the handling and positioning of the sensor in the bench setup, and the precision limit of consecutive measurements without handling or changing the sensor corresponds to only 0.66% of the mean measurement.

C. Sensor Sensitivity

To guarantee the quality of the waveform morphology and its parameters, the sensor must have a nanometric resolution. Displacements must be distinguishable at a level of 1% of cranial expansion. The sensitivity of the sensor was tested using SETAS to produce nanometric dynamic displacements against the sensitive pin of the sensor. Initially, SETAS was programmed to reproduce 10 steps of 500 nm , resulting in a total displacement of $5 \mu\text{m}$. For this test, a closed-loop mode was used, and the displacements were controlled using an optical encoder as the position feedback.

Before starting the steps, the initial position of the actuator was $200 \mu\text{m}$ beyond the threshold where the actuator touched the pin of the sensor. The signal was detrended using a linear equation considering the initial and final position readings and scaled to match the encoder readings. The readings from the wireless sensor and encoder are compared in Figure 13a. The y-axes have the same span, but the limits were offset to make the plots more visible.

Next, the sensor was tested back and forth with cycles of 10 steps of 40 nm using SETAS in closed-loop mode. The encoder and wireless sensor signals are shown in Figure 13b.

The change in the signal caused by a displacement of 40 nm was visually distinguishable. The mean standard deviation in 1 s of data for all segments in five cycles was 9.124 nm . A confidence interval of ± 3 signals is then equivalent to a deviance interval of $\pm 27.372 \text{ nm}$ in the sensor readings, and a confidence interval of ± 2 sigmas results in a deviance of $\pm 18.248 \text{ nm}$. Defining the resolution as four sigmas, which results in a probability of 4.6% that a sample lies outside of the range, during this test a resolution of 36.496 nm was obtained. A 4 sigmas interval is illustrated in Figure 13c, where the red box height indicates the interval enclosing the signal read by the sensor between a step of 40 nm .

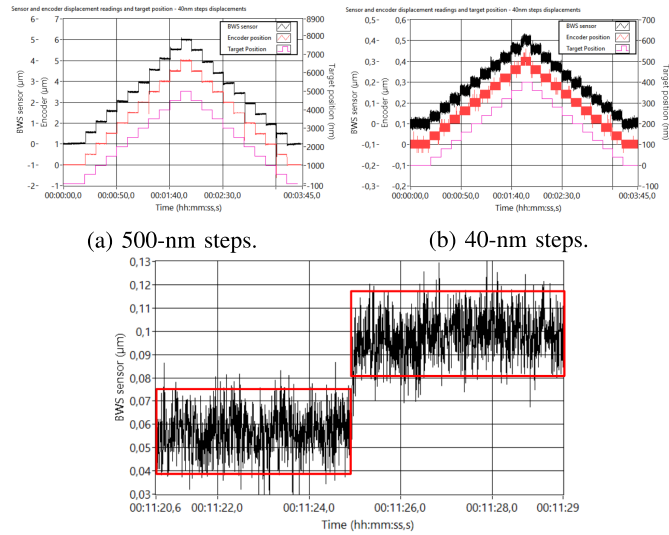
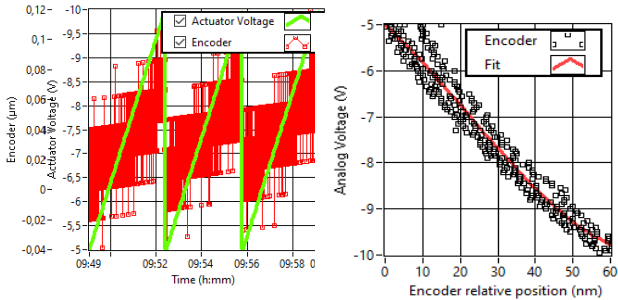


Fig. 13. (a) Signal obtained from 10 displacements of 500 nm (b). Signal obtained from 10 displacements of 40 nm. (c) Step of 40 nm in close up. The red box represents the interval of 4 standard deviations.



(a) Voltage applied to excite the actuator and the encoder displacement reading. (b) Calibration curve using a third-order polynomial equation.

Fig. 14. (a) Illustrates the voltage applied to excite the actuator and the encoder displacement readings. These data were used to obtain the calibration curve in (b).

To test the sensor’s response for displacements of 4 nm, SETAS was configured to work in open-loop mode, because the encoder used to control the position in closed-loop mode has a digital resolution of 20 nm. In this test, the displacements were controlled only by specifying the analog voltage that would excite the piezoelectric actuator.

Because the position was not controlled directly, a voltage-to-displacement calibration curve was obtained. The actuator was excited within the range of -5 to -10 V in steps of 50 mV and 2 s, and the mean measurement of the encoder during the middle 1 s (100 samples) of each step was recorded.

Figure 14a shows the applied excitation voltage of the actuator and the raw readings of the encoder. Figure 14b shows the calibration curve obtained by fitting a third-order polynomial equation, where each point on the graph represents the mean reading of the middle 1 s (100 samples) of each step.

SETAS was programmed to perform five cycles of ten 4-nm positive and negative steps using the polynomial

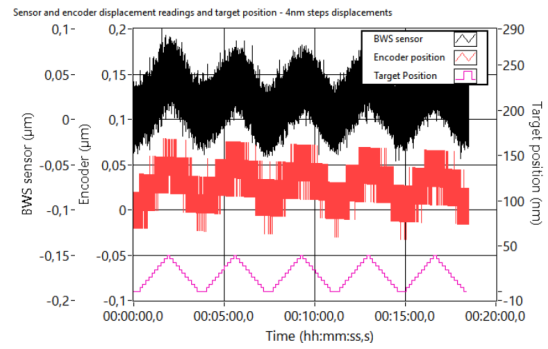


Fig. 15. Signals obtained by the sensor and the encoder as SETAS sets the target position in 4-nm steps.

TABLE VI
COMPARISON OF THE NORMAL WAVEFORM CHARACTERISTICS BASED ON THE ENCODER READINGS AND THE SIGNAL OBTAINED BY THE SENSOR

Typical ICP waveform simulation						
Characteristics of the waveform performed by SETAS						
Waveform morphology						
P2/P1 ratio	0.90	0.90	0.90	0.92	0.96	1.00
Heart rate (BPM)	50	79	98	119	146	176
TTP (s)	0.08	0.09	0.09	0.09	0.12	0.14
Characteristics of the waveform obtained by the sensor						
Waveform morphology						
P2/P1 ratio	0.88	0.89	0.90	0.93	0.96	1.00
Heart rate (BPM)	50	79	101	118	146	176
TTP (s)	0.10	0.09	0.09	0.09	0.12	0.14

equation obtained from the calibration. The actuator was maintained for 10 s in each step level. After detrending the signal using a linear equation considering equal initial and final values of the acquisition and scaling the obtained signal in $\mu\text{V}/\text{V}$ to match the maximum amplitude obtained by the encoder in μm , the signals are as presented in Figure 15.

To better visualize the readings, Figure 16 shows the boxplot of one of each step level cycle from both the sensor and encoder readings. The data used to compute the boxplots were sequential readings in an interval of 1 s, 8.5 s after the step occurs. Because of the digital resolution limit of the position encoder, the first, second, and third quartiles are coincident in some of the encoder readings. In addition, the nuances were more distinguishable in the wireless sensor boxplot. At this level, it is difficult to check if the steps are performed correctly owing to the encoder resolution limit.

D. Comparison of Waveform Characteristics

To test the dynamic behavior of the sensor when compared with the absolute pin deflection, two types of NIICP waveforms were simulated using SETAS and read by the sensor and absolute encoder for 3 min. The BWS generates reports for each waveform signal. The frequency (heart rate) of each waveform varied from 50 to 180 bpm, and the amplitude was constant at 10 μm . One minute of data for each waveform

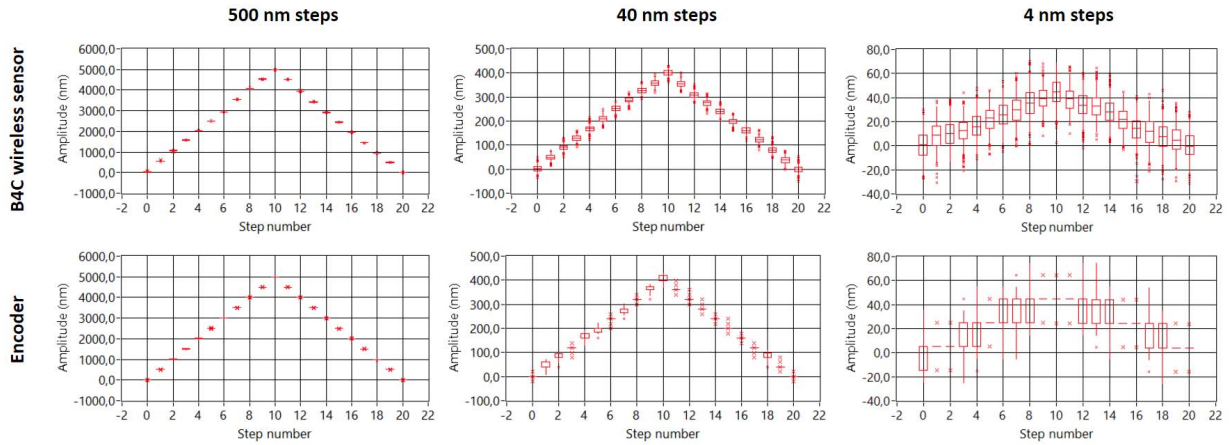


Fig. 16. Wireless sensor and encoder boxplot comparison for a cycle of 500-, 40-, and 4-nm steps.

TABLE VII
COMPARISON OF PATHOLOGICAL WAVEFORM CHARACTERISTICS
BASED ON THE ENCODER READINGS AND THE SIGNAL
OBTAINED BY THE SENSOR

Pathological waveform simulation						
Characteristics of the waveform performed by SETAS						
Waveform morphology						
P2/P1 ratio	1.11	1.11	1.12	1.15	1.15	1.16
Heart rate (BPM)	50	79	98	118	146	176
TTP (s)	0.26	0.26	0.27	0.27	0.26	0.26
Characteristics of the waveform obtained by the sensor						
Waveform morphology						
P2/P1 ratio	1.10	1.10	1.10	1.12	1.13	1.14
Heart rate (BPM)	50	79	98	118	146	176
TTP (s)	0.27	0.27	0.27	0.27	0.28	0.26

frequency was analyzed, and the parameters of the P2/P1 ratio, heart rate, and normalized TTP as achieved by SETAS were compared to the parameters obtained by the sensor.

Owing to the limitation of 100 position writings/s used to reproduce the waveform, some details of the waveform morphology were affected when the heart rate of the waveform was increased. Nevertheless, the relation between the waveforms obtained from the encoder and sensor is still close, with a maximum deviation of 0.03 (2.6%) in the P2/P1 relation of the pathological waveform of 118 bpm. It is worth noting that there are a few elements that can contribute to such differences, including the damping that may occur between the mechanical elements of SETAS and the processing algorithms. Tables VI and VII summarize the characteristics of the signal read by the optical encoder and the signal obtained by the wireless sensor.

VII. DISCUSSION

A. NIICP Signal Scale Comparison

For comparative purposes, Figure 17 demonstrates the magnitude of some common examples and compares them with the values analyzed in this study. The skull deformation (5 μm) translated into the average NIICP waveform amplitude is one-tenth the diameter of a human hair and is invisible to the

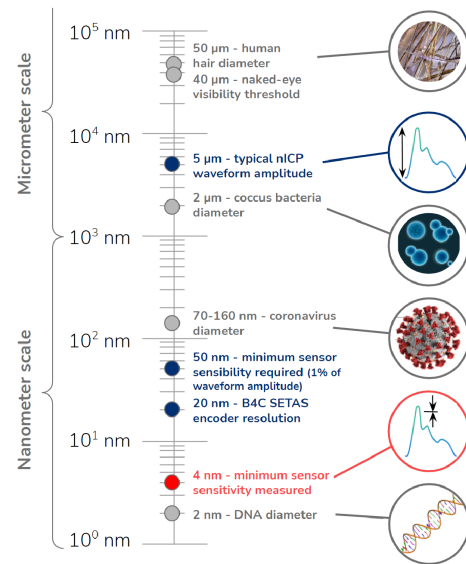


Fig. 17. Logarithm scale comparison for sensor sensitivity.

naked eye. Furthermore, as described in Section VI, the system demonstrated an excellent precision and sensibility, perceiving up to 4 nm of displacement, a scale that is comparable to a DNA diameter (2 nm). When considering the amount of noise and the level of stability, the sensor was capable of distinguishing level differences of 40 nm with a confidence of greater than 95%.

B. NIICP Waveform Integrity and Analysis

In addition to the current Bluetooth® standard, a proprietary Bluetooth® protocol was designed to guarantee the integrity of the communication signal and to avoid errors caused by a weak signal strength between devices owing to obstacles or distance. It identifies points that were lost considering the moment at which these losses occurred, thus avoiding distortions in the original waves. The comparison between the signals is presented in Table VIII, indicating waveform data without loss of points, with 1%, 5%, and 10% loss.

The results show that even when 10% of the points are lost, the NIICP waveform characteristics mostly do not change. Tests checking for data loss on the BWS were executed to explore critical scenarios beyond those specified for its

TABLE VIII

EXAMPLE OF NIICP WAVEFORM WITH DATA LOSS, THE FIRST SIGNAL WITHOUT LOSS, THE SECOND LOSING 1%, THE THIRD LOSING 5%, AND THE FOURTH LOSING 10% OF DATA (RANDOMLY CREATED)

Comparison between waveform when losing points				
Characteristics of the waveform with lost of data				
Waveform morphology with loss of data				
Percentage of data loss	0%	1%	5%	10%
Result with 1 minute of data with that point loss rate				
P2/P1 ratio	0.92	0.94	0.94	0.94
TTP (s)	0.22	0.22	0.22	0.22

use. Signal acquisition was performed five times, each with a 1-h duration, with three different sets of equipment, at a 15-m distance between the sensor and receiver inside a closed environment. Monitoring sessions showed that the waveform integrity had less than 1% data loss, even at distances three-times greater than that originally recommended, ensuring the signal quality.

C. Wireless Sensor Contributions

Some improvements and contributions of wireless sensor is described below:

- 1) *Signal reliability*: By calibrating into displacement measures, the wireless sensor improves the reproducibility of the system, making it possible to compare the results between sensors and patient monitoring sessions. In addition, considering the resolution as a level difference that is distinguishable 95.4% of the time or more, the goal of less than 1% of a typical NIICP signal resolution was achieved, as demonstrated in the tests described in Section VI. Furthermore, no post-process filtering was used during the sensitivity test, indicating that a better signal can be achieved without compromising important information, typically at under 18 Hz.
- 2) *Usability*: Compared to the wired version, the wireless sensor is easier to use, enhances the mobility, makes the positioning easier, has less risk of failure, and results in less patient discomfort.
- 3) *Integration with other systems*: Wireless communication in real time with patient monitors and mobile device applications simultaneously makes possible multiple applications. In addition, cloud integration generates reports faster than the previous system and allows physicians to access them remotely.

D. Limitations and Opportunities

The device presented here sheds light on new roads in neurological monitoring for healthcare professionals. Improving the usability will directly affect how the sensor is handled, reducing errors, and making it more efficient and effective. For this reason, some issues need to be considered:

- 1) *Operator dependency*: Like any other sensor (e.g., EKG, Doppler ultrasonography sensor), the signal obtained may partially depend on the operator and the sense to distinguish if it is correctly positioned. Improving the

instantaneous feedback of the sensor positioning may greatly reduce the time spent adjusting the sensor in the patient's head and improving the signal quality at the same time.

- 2) *Sensor positioning and fixing*: Special care must be taken when monitoring people in a delicate condition because of the tension generated in the headband when fixing the sensor. The sensor is contraindicated and may be harmful to patients with fractures of the skull or who underwent decompressive craniectomy (removal of a bone flap from the skull). When considering patients with cranial malformations and neonatal and premature application, not only should the headband tension be considered, but the headband should also be able to adjust to the size of the head circumference. Developing alternative ways to fix the sensor will make NIICP monitoring more accessible and safer. In addition, physical behavior of the skull in these cases may differ from the behavior observed in a completely developed and closed skull, requiring further study.
- 3) *External influences*: Both the mechanical and electronic parts of the sensor may be affected by external influences. The patient's involuntary or voluntary motion can be transmitted to the cantilever beam mechanism, which responds to displacements. The movements transmitted from the headband to the sensor's housing when the sensor is not positioned correctly can also attenuate the signal perceived by the sensor. Compensation algorithms using an embedded 9-axes IMU can be improved. Another possible motion source is the peripheral blood circulation, and a study using technologies such as plethysmography could be conducted to check its influence on the sensor measurements. Such measurements will increase the signal quality and reduce the number of data recollections owing to a poor quality acquisition. Usually, changes in the system temperature will not affect the NIICP parameters obtained because abrupt changes in temperature are not expected in a one-pulse interval, and small thermal drifts can be treated with a detrending algorithm before processing the NIICP parameters.
- 4) *System test limitation*: Within SETAS, the position encoder resolution used in the test was 20 nm, preventing the system from having a direct position feedback for displacements under this limit. The position reading/writing rate also affects the waveform morphology when simulating higher heart-rate NIICP pulses. For tests beyond these limits, new methodologies or other equipment are necessary.
- 5) *Sensor and headband size*: Headband and wireless sensor sizes are in development to monitor infants (0 to 36 months of age) for cephalic perimeters smaller than 40 cm. In addition, the infant skull has fontanelles, membranes that separate cranial bones, which could have a different physical behavior compared to adult skulls (consolidated cranial vault). Monitoring children is also delicate because they have difficulties in remaining still, which creates artifacts and disturbances in the signal. Hence, applications of the NIICP method for the

pediatric population must still be validated, considering a possible compact format of the sensor and signal compensation against movement.

E. New Applications

Apart from a physical examination, healthcare professionals can support their therapeutic decisions using this low-risk device by receiving real-time information, thereby adding one more piece to the clinical assessment puzzle. The possibility of monitoring the ICP and intracranial compliance with this new noninvasive method can enhance not only clinical practice inside and outside healthcare services but also deepen studies regarding conditions affecting the CNS. Some of the possibilities to mention here, in addition to the current IICP limitations [30], [34]–[39], would be to improve the quality of life of people with neurological disorders [80], [81] and achieve a differential diagnosis for migraines and other CNS dysfunctions [82]–[84], less painful procedures for the pediatric population [85], a continuous follow-up of pseudotumor cerebri condition in which there is no mass-affecting lesion but where the ICP is elevated using less invasive procedures [86], and even further studies on microgravity repercussion on the CNS for spaceflight [87]–[89]. Indeed, until now, the situation has not been conducive to measuring this physiological parameter in a traditionally invasive way.

VIII. CONCLUSION

The new comprehension of Monro–Kellie doctrine led to the development of a new method for monitoring ICP and intracranial compliance based on nanometric cranial expansions. The design and characterization of a commercially available, wireless, non-invasive ICP monitoring sensor is described in this paper.

Non-invasiveness mitigates certain risks, including lesions and infections, to patients. Because the proposed sensor is portable and wireless, it is also very cost-accessible and easy to use. The device was approved by the Brazilian Health Regulatory Agency (Anvisa) (registration number 81157910004) and has already been applied in many hospitals. Currently, the wired version is already FDA approved (registered under 510(K) Number K182073), and the wireless version is under the certification process. The device and NIICP method described in this article are both patented (US-9826934, USA; US-9993170-B1, USA; EP2757939 B1, Europe).

With a digitization of the signal and integration with the cloud and analytics tools, the system enables visualizing, recording, and obtaining valuable information regarding intracranial compliance in a fast and easy way. The monitoring reports are also accessible through the Internet and can be shared with authorized individuals, allowing the patient, physician, or researcher to easily acquire a second opinion.

Methods for testing and validating the sensor were also developed because the standards available for ICP sensors are aimed at traditional invasive sensors. Three important competencies were evaluated in the sensor: stability of the measurements, nanometric sensitivity, and waveform parameters reproduction. The results show that the sensor is sufficiently sensitive to distinguish displacements with a magnitude of 1% of the amplitude of a cranial expansion pulse, making

it an essential method for delivering a consistent waveform morphology to a clinical interpretation [90].

This paper describes the working principle of the sensor, its benefits, and its main characteristics, allowing researchers and physicians to understand the variable being monitored and to evaluate its use in their applications.

REFERENCES

- [1] C. C. Leite, E. Amaro, Jr., and L. T. Lucato, *Neuroradiologia: Diagnóstico Por Imagem Das Alterações Encefálicas*. Rio de Janeiro, Brazil: Guanabara Koogan, 2008.
- [2] V. Petrik, V. Apok, J. A. Britton, B. A. Bell, and M. C. Papadopoulos, “Godfrey Hounsfield and the dawn of computed tomography,” *Neurosurgery*, vol. 58, pp. 780–786, Apr. 2006.
- [3] R. Zimmerman, W. Gibby, and R. Carmody, *Neuroimaging: Clinical and Physical Principles*. New York, NY, USA: Springer-Verlag, Jan. 2000.
- [4] E.-W. Radue, M. Weigel, R. Wiest, and H. Urbach, “Introduction to magnetic resonance imaging for neurologists,” *CONTINUUM, Lifelong Learn. Neurol.*, vol. 22, no. 5, pp. 1379–1398, Oct. 2016.
- [5] N. K. Pinter and J. V. Fritz, “Neuroimaging for the neurologist: Clinical MRI and future trends,” *Neurolog. Clinics*, vol. 38, no. 1, pp. 1–35, Feb. 2020.
- [6] B. Young *et al.*, “Cerebral microdialysis,” *Crit. Care Nursing Clinics*, vol. 28, no. 1, pp. 109–124, 2016.
- [7] Z. Guo, M. C.-W. Leong, H. Su, K.-W. Kwok, D. T.-M. Chan, and W.-S. Poon, “Techniques for stereotactic neurosurgery: Beyond the frame, toward the intraoperative magnetic resonance imaging-guided and robot-assisted approaches,” *World Neurosurg.*, vol. 116, pp. 77–87, Aug. 2018.
- [8] D. A. Orringer, A. Golby, and F. Jolesz, “Neuronavigation in the surgical management of brain tumors: Current and future trends,” *Expert Rev. Med. Devices*, vol. 9, no. 5, pp. 491–500, Sep. 2012.
- [9] M. Roth and L. Rakers, “Intraoperative neuromonitoring: Principles and considerations for perioperative nurses,” *AORN J.*, vol. 110, no. 1, pp. 11–26, Jul. 2019.
- [10] W. Ishida *et al.*, “Diagnostic and therapeutic values of intraoperative electrophysiological neuromonitoring during resection of intradural extramedullary spinal tumors: A single-center retrospective cohort and meta-analysis,” *J. Neurosurg., Spine*, vol. 30, no. 6, pp. 839–849, Jun. 2019.
- [11] P. J. Bassler, S. Pajevic, C. Pierpaoli, J. Duda, and A. Aldroubi, “*In vivo* fiber tractography using DT-MRI data,” *Magn. Reson. Med.*, vol. 44, no. 4, pp. 625–632, 2000.
- [12] R. Ito, S. Mori, and E. R. Melhem, “Diffusion tensor brain imaging and tractography,” *Neuroimaging Clinics North Amer.*, vol. 12, no. 1, pp. 1–19, 2002.
- [13] D. Stein *et al.*, “3D virtual reconstruction and quantitative assessment of the human intervertebral disc’s annulus fibrosus: A DTI tractography study,” *Sci. Rep.*, vol. 11, no. 1, pp. 1–11, Dec. 2021.
- [14] J. C. Sigl and N. G. Chamoun, “An introduction to bispectral analysis for the electroencephalogram,” *J. Clin. Monit.*, vol. 10, no. 6, pp. 392–404, 1994.
- [15] C. R. D. Oliveira, W. M. Bernardo, and V. M. Nunes, “Benefit of general anesthesia monitored by bispectral index compared with monitoring guided only by clinical parameters. Systematic review and meta-analysis,” *Brazilian J. Anesthesiology (English Ed.)*, vol. 67, no. 1, pp. 72–84, Jan. 2017.
- [16] C. Rosow and P. J. Manberg, “Bispectral index monitoring,” *Anesthesiology Clinics North Amer.*, vol. 19, no. 4, pp. 947–966, 2001.
- [17] F. Scholkmann *et al.*, “A review on continuous wave functional near-infrared spectroscopy and imaging instrumentation and methodology,” *NeuroImage*, vol. 85, pp. 6–27, Jan. 2014.
- [18] M. Ferrari and V. Quaresima, “A brief review on the history of human functional near-infrared spectroscopy (fNIRS) development and fields of application,” *NeuroImage*, vol. 63, no. 2, pp. 921–935, Nov. 2012.
- [19] R. Aaslid, T.-M. Markwalder, and H. Nornes, “Noninvasive transcranial Doppler ultrasound recording of flow velocity in basal cerebral arteries,” *J. Neurosurg.*, vol. 57, no. 6, pp. 769–774, Dec. 1982.
- [20] H. L. Edmonds, M. R. Isley, T. B. Sloan, A. V. Alexandrov, and A. Y. Razumovsky, “American society of neurophysiologic monitoring and American society of neuroimaging joint guidelines for transcranial Doppler ultrasonic monitoring,” *J. Neuroimag.*, vol. 21, no. 2, pp. 177–183, Apr. 2011.
- [21] N. Carney *et al.*, “Guidelines for the management of severe traumatic brain injury,” *Neurosurgery*, vol. 80, no. 1, pp. 6–15, 2016.

- [22] G. Kellie, "An account of the appearances observed in the dissection of two of three individuals presumed to have perished in the storm of the 3D, and whose bodies were discovered in the vicinity of leith on the morning of the 4th, November 1821; with some reflections on the pathology of the brain: Part I," *Trans. Medico-Chirurgical Soc. Edinburgh*, vol. 1, pp. 84–122, Nov. 1824.
- [23] M. H. Wilson, "Monro-kellie 2.0: The dynamic vascular and venous pathophysiological components of intracranial pressure," *J. Cerebral Blood Flow Metabolism*, vol. 36, no. 8, pp. 1338–1350, Aug. 2016.
- [24] J. Hall and M. Hall, *Guyton and Hall Textbook of Medical Physiology*. Amsterdam, The Netherlands: Elsevier, 2021.
- [25] N. Lundberg, "Continuous recording and control of ventricular fluid pressure in neurosurgical practice," *J. Neuropathology Experim. Neurol.*, vol. 21, no. 3, p. 489, Jul. 1962.
- [26] N. Lundberg, "The saga of the Monro-Kellie doctrine," in *Intracranial Pressure*, V. S. Ishii, H. Nagel, and M. Brock, Eds. Berlin, Germany: Springer, 1983, pp. 68–76.
- [27] E. Kandel, S. Mack, T. Jessell, J. Schwartz, S. Siegelbaum, and A. Hudspeth, *Principles of Neural Science*, 5th ed. New York, NY, USA: McGraw-Hill, 2015.
- [28] E. Marcolini, C. Stretz, and K. M. DeWitt, "Intracranial hemorrhage and intracranial hypertension," *Emergency Med. Clinics North Amer.*, vol. 37, no. 3, pp. 529–544, Aug. 2019.
- [29] Z. Czosnyka and M. Czosnyka, "Long-term monitoring of intracranial pressure in normal pressure hydrocephalus and other CSF disorders," *Acta Neurochirurgica*, vol. 159, no. 10, pp. 1979–1980, Oct. 2017.
- [30] D. S. Nag, S. Sahu, A. Swain, and S. Kant, "Intracranial pressure monitoring: Gold standard and recent innovations," *World J. Clin. Cases*, vol. 7, no. 13, pp. 1535–1553, Jul. 2019.
- [31] A. K. Filis, K. Aghayev, and F. D. Vrionis, "Cerebrospinal fluid and hydrocephalus: Physiology, diagnosis, and treatment," *Cancer Control*, vol. 24, no. 1, pp. 6–8, Jan. 2017.
- [32] T. Schizodimos, V. Soulountsi, C. Iasonidou, and N. Kapravelos, "An overview of management of intracranial hypertension in the intensive care unit," *J. Anesthesia*, vol. 34, no. 5, pp. 741–757, Oct. 2020.
- [33] J. D. Robinson, "Management of refractory intracranial pressure," *Crit. Care Nursing Clinics North Amer.*, vol. 28, no. 1, pp. 67–75, Mar. 2016.
- [34] M. Harary, R. G. Dolmans, and W. B. Gormley, "Intracranial pressure monitoring—Review and avenues for development," *Sensors*, vol. 18, no. 2, p. 465, 2018.
- [35] R. Ma *et al.*, "Complications following intracranial pressure monitoring in children: A 6-year single-center experience," *J. Neurosurg., Pediatrics*, vol. 21, no. 3, pp. 278–283, Mar. 2018.
- [36] S. Tavakoli, G. Peitz, W. Ares, S. Hafeez, and R. Grandhi, "Complications of invasive intracranial pressure monitoring devices in neurocritical care," *Neurosurgical Focus*, vol. 43, no. 5, p. E6, Nov. 2017.
- [37] J. Vaquero *et al.*, "Complications and use of intracranial pressure monitoring in patients with acute liver failure and severe encephalopathy," *Liver Transplantation*, vol. 11, no. 12, pp. 1581–1589, 2005.
- [38] A. A. Rabinstein, "Treatment of brain edema in acute liver failure," *Current Treatment Options Neurol.*, vol. 12, no. 2, pp. 129–141, Mar. 2010.
- [39] A. T. Blei, "Brain edema in acute liver failure: Can it be prevented? Can it be treated?" *J. Hepatol.*, vol. 46, no. 4, pp. 564–569, Apr. 2007.
- [40] S. Agerskov, M. Wallin, P. Hellström, D. Ziegelitz, C. Wikkelsö, and M. Tullberg, "Absence of disproportionately enlarged subarachnoid space hydrocephalus, a sharp callosal angle, or other morphologic MRI markers should not be used to exclude patients with idiopathic normal pressure hydrocephalus from shunt surgery," *Amer. J. Neuroradiol.*, vol. 40, no. 1, pp. 74–79, Jan. 2019.
- [41] J. Bellner, B. Romner, P. Reinstrop, K.-A. Kristiansson, E. Ryding, and L. Brandt, "Transcranial Doppler sonography pulsatility index (PI) reflects intracranial pressure (ICP)," *Surgical Neurol.*, vol. 62, no. 1, pp. 45–51, Jul. 2004.
- [42] A. D'Andrea *et al.*, "Transcranial Doppler ultrasonography: From methodology to major clinical applications," *World J. Cardiol.*, vol. 8, no. 7, p. 383, 2016.
- [43] C. Hylkema, "Optic nerve sheath diameter ultrasound and the diagnosis of increased intracranial pressure," *Crit. Care Nursing Clinics North Amer.*, vol. 28, no. 1, pp. 95–99, Mar. 2016.
- [44] C. Robba *et al.*, "Optic nerve sheath diameter measured sonographically as non-invasive estimator of intracranial pressure: A systematic review and meta-analysis," *Intensive Care Med.*, vol. 44, no. 8, pp. 1284–1294, Aug. 2018.
- [45] C. M. Campbell-Bell, A. A. Birch, D. Vignali, D. Bulters, and R. J. Marchbanks, "Reference intervals for the evoked tympanic membrane displacement measurement: A non-invasive measure of intracranial pressure," *Physiol. Meas.*, no. 1, p. 19, Jan. 2018.
- [46] W. K. El-Bouri *et al.*, "Quantifying the contribution of intracranial pressure and arterial blood pressure to spontaneous tympanic membrane displacement," *Physiol. Meas.*, vol. 39, no. 8, Aug. 2018, Art. no. 085002.
- [47] S. Oliveira *et al.*, "The new ICP minimally invasive method shows that the Monro-Kellie doctrine is not valid," *Acta Neurochirurgica. Suppl.*, vol. 114, pp. 20–117, Jan. 2012.
- [48] D. Felten, M. O'Banion, and M. Maida, "Netter's atlas of neuroscience," in *Netter Basic Science*. Amsterdam, The Netherlands: Elsevier, 2014.
- [49] M. Siqueira, *Tratado De Neurocirurgia*. Manila, Philippines: Manole, 2015.
- [50] N. Carney *et al.*, "Guidelines for the management of severe traumatic brain injury," *Neurosurgery*, vol. 80, no. 1, pp. 6–15, 2016.
- [51] R. D. Stevens, M. Shoykhet, and R. Cadena, "Emergency neurologic life support: Intracranial hypertension and herniation," *Neurocrit. Care*, vol. 23, no. S2, pp. 76–82, Dec. 2015.
- [52] *Advanced Trauma Life Support: ATLS Student Course Manual*, American College of Surgeons, Chicago, IL, USA, 2018.
- [53] A. Meyer, "Herniation of the brain," *Arch. Neurol. Psychiatry*, vol. 4, no. 4, pp. 387–400, 1920.
- [54] A. Marmarou, K. Shulman, and J. LaMorgese, "Compartmental analysis of compliance and outflow resistance of the cerebrospinal fluid system," *J. Neurosurg.*, vol. 43, no. 5, pp. 523–534, Nov. 1975.
- [55] C. Hawthorne and I. Piper, "Monitoring of intracranial pressure in patients with traumatic brain injury," *Frontiers Neurol.*, vol. 5, p. 121, Jul. 2014.
- [56] M. Czosnyka and Z. Czosnyka, "Origin of intracranial pressure pulse waveform," *Acta Neurochirurgica*, vol. 162, no. 8, pp. 1815–1817, Aug. 2020.
- [57] K. B. Evensen, K. Paulat, F. Prieur, S. Holm, and P. K. Eide, "Utility of the tympanic membrane pressure waveform for non-invasive estimation of the intracranial pressure waveform," *Sci. Rep.*, vol. 8, no. 1, pp. 1–11, Dec. 2018.
- [58] K. B. Evensen and P. K. Eide, "Mechanisms behind altered pulsatile intracranial pressure in idiopathic normal pressure hydrocephalus: Role of vascular pulsatility and systemic hemodynamic variables," *Acta Neurochirurgica*, vol. 162, no. 8, pp. 1803–1813, Aug. 2020.
- [59] P. K. Eide and W. Sorteberg, "Intracranial pressure levels and single wave amplitudes, glasgow coma score and glasgow outcome score after subarachnoid haemorrhage," *Acta Neurochirurgica*, vol. 148, no. 12, pp. 1267–1275, Dec. 2006.
- [60] M. D. Okon *et al.*, "Characteristics of the cerebrospinal fluid pressure waveform and craniospinal compliance in idiopathic intracranial hypertension subjects," *Fluids Barriers CNS*, vol. 15, no. 1, pp. 1–7, Aug. 2018.
- [61] E. Carrera *et al.*, "What shapes pulse amplitude of intracranial pressure?" *J. Neurotrauma*, vol. 27, no. 2, pp. 317–324, Feb. 2010.
- [62] X. Hu, P. Xu, F. Scalzo, P. Vespa, and M. Bergsneider, "Morphological clustering and analysis of continuous intracranial pressure," *IEEE Trans. Biomed. Eng.*, vol. 56, no. 3, pp. 696–705, Mar. 2009.
- [63] I. Martinez-Tejada, A. Arum, J. E. Wilhjelm, M. Juhler, and M. Andresen, "B waves: A systematic review of terminology, characteristics, and analysis methods," *Fluids Barriers CNS*, vol. 16, no. 1, pp. 1–15, 2019.
- [64] C. J. Kirkness, P. H. Mitchell, R. L. Burr, K. S. March, and D. W. Newell, "Intracranial pressure waveform analysis: Clinical and research implications," *J. Neurosci. Nursing*, vol. 32, no. 5, pp. 271–277, Oct. 2000.
- [65] E. R. Cardoso, J. O. Rowan, and S. P. Galbraith, "Analysis of the cerebrospinal fluid pulse wave in intracranial pressure," *J. Neurosurgery*, vol. 59, no. 5, pp. 817–821, 1983.
- [66] D. J. Doyle and P. W. Mark, "Analysis of intracranial pressure," *J. Clin. Monitor.*, vol. 8, no. 1, pp. 81–90, 1992.
- [67] K. Germon, "Interpretation of ICP pulse waves to determine intracerebral compliance," *J. Neurosci. Nursing*, vol. 20, no. 6, pp. 344–351, Dec. 1988.
- [68] J. Arroyo-Palacios *et al.*, "Characterization of shape differences among ICP pulses predicts outcome of external ventricular drainage weaning trial," *Neurocrit. Care*, vol. 25, no. 3, pp. 424–433, Dec. 2016.
- [69] O. Hirai, H. Handa, M. Ishikawa, and S.-H. Kim, "Epidural pulse waveform as an indicator of intracranial pressure dynamics," *Surgical Neurol.*, vol. 21, no. 1, pp. 67–74, Jan. 1984.
- [70] T. Tokutomi *et al.*, "Analysis of pulse wave recorded on epidural pressure in acute intracranial hypertension," *Neurologia Medico-Chirurgica*, vol. 25, no. 6, pp. 418–424, 1985.

- [71] M. Shigemori, T. Tokutomi, T. Kawaba, H. Nakashima, and S. Kuramoto, "Analysis of epidural pressure pulse wave (EDP-PW) and common carotid blood velocity (CBFV) in acute intracranial hypertension," *Neurolog. Res.*, vol. 8, no. 2, pp. 105–108, Jun. 1986.
- [72] M. Shigemori, T. Kawaba, T. Tokutomi, H. Nakashima, T. Yuge, and S. Kuramoto, "Analysis of pulse waves of epidural pressure recorded in acute intracranial hypertension: Amplitude changes of pulse wave components and their clinical significance," *Neurologia Medico-Chirurgica*, vol. 27, no. 4, pp. 289–294, 1987.
- [73] P. K. Eide, "Assessment of childhood intracranial pressure recordings using a new method of processing intracranial pressure signals," *Pediatric Neurosurg.*, vol. 41, no. 3, pp. 122–130, 2005.
- [74] R. Andrade, "Analysis and improvement of a non-invasive intracranial pressure monitoring system," M.S. thesis, Dept. Mech. Eng., Univ. Sao Paulo, Sao Carlos, Brazil, 2013.
- [75] G. Frigieri *et al.*, "Analysis of a non-invasive intracranial pressure monitoring method in patients with traumatic brain injury," *Acta Neurochirurgica, Supplementum*, vol. 126, pp. 107–110, 2018.
- [76] B. Cabella *et al.*, "Validation of a new noninvasive intracranial pressure monitoring method by direct comparison with an invasive technique," *Acta Neurochirurgica Supplement*, pp. 93–96, 2016.
- [77] G. Frigieri *et al.*, "Analysis of a non-invasive intracranial pressure monitoring method in patients with traumatic brain injury," *Acta Neurochirurgica, Supplementum*, vol. 126, pp. 107–110, 2018.
- [78] G. H. F. Vilela, "Development of a minimally invasive system to monitor the intracranial pressure," Ph.D. dissertation, Sao Carlos Inst. Phys., Univ. Sao Paulo, Sao Carlos, Brazil, 2010.
- [79] *Blood Pressure Transducer*, document ANSI/AAMI BP22:1994 (R)2016, American National Standard, Geneva, Switzerland, 2016.
- [80] B. Lindquist, E. Fernell, E.-K. Persson, and P. Uvebrant, "Quality of life in adults treated in infancy for hydrocephalus," *Child's Nervous Syst.*, vol. 30, no. 8, pp. 1413–1418, Aug. 2014.
- [81] V. L. Feigin *et al.*, "The global burden of neurological disorders: Translating evidence into policy," *Lancet Neurol.*, vol. 19, no. 3, pp. 255–265, Mar. 2020.
- [82] M. Torbey, R. Geocadin, A. Razumovsky, D. Rigamonti, and M. Williams, "Utility of CSF pressure monitoring to identify idiopathic intracranial hypertension without papilledema in patients with chronic daily headache," *Cephalalgia*, vol. 24, no. 6, pp. 495–502, Jun. 2004.
- [83] M. Togha *et al.*, "Prevalence of new-onset migraine in patients with idiopathic intracranial hypertension in comparison to the general population," *Iranian J. Neurol.*, vol. 17, no. 4, p. 161, 2018.
- [84] R. E. Ryan and S. H. Pearlman, "Common headache misdiagnoses," *Primary Care, Clinics Office Pract.*, vol. 31, no. 2, pp. 395–405, Jun. 2004.
- [85] E. B. Lee, F. S. Edelman, and C. E. Stafstrom, "Evidence of diplopia in children's headache drawings helps to differentiate pseudotumor cerebri from migraine," *Pediatric Neurol.*, vol. 79, pp. 40–44, Feb. 2018.
- [86] R. M. Mallery, D. I. Friedman, and G. T. Liu, "Headache and the pseudotumor cerebri syndrome," *Current Pain Headache Rep.*, vol. 18, no. 9, p. 446, Sep. 2014.
- [87] J. S. Lawley *et al.*, "Effect of gravity and microgravity on intracranial pressure," *J. Physiol.*, vol. 595, no. 6, pp. 2115–2127, Mar. 2017.
- [88] K. Iwasaki *et al.*, "Long-duration spaceflight alters estimated intracranial pressure and cerebral blood velocity," *J. Physiol.*, vol. 599, no. 4, pp. 1067–1081, Feb. 2021.
- [89] D. Alexander *et al.*, "NASA evidence report: Risk of spaceflight-induced intracranial hypertension and vision alterations," Lyndon B. Johnson Space Center, Nat. Aeronaut. Space Admin., Houston, TX, USA, Tech. Rep., 2012.
- [90] *Intracranial Pressure Monitoring Devices*, document ANSI/AAMI NS28:1988 (R)2015, American National Standard, Arlington, TX, USA, 2015.

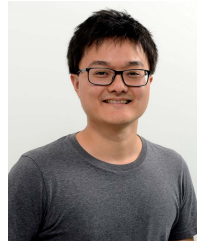


Rodrigo de A. P. Andrade (Member, IEEE) received the B.S. degree in control and automation engineering from the Centro Federal de Educação Tecnológica de Minas Gerais, Leopoldina, Brazil, in 2010, and the M.S. degree in mechanical engineering from the University of Sao Paulo, São Carlos, Brazil, in 2013, where he is currently pursuing the Ph.D. degree in electrical engineering. He is a Co-Founder, a Responsible Engineer in Charge, and the Product Development Director at Braincare Desenvolvimento e Inovação Tecnológica S.A., working on the development of medical products. He has experience in medical devices, industrial automation, with an emphasis on embedded instrumentation, acting mainly on the following topics, such as medical instrumentation, sensors, wireless data acquisition, optogenetic instrumentation, and automated test systems development.

working on the development of medical products. He has experience in medical devices, industrial automation, with an emphasis on embedded instrumentation, acting mainly on the following topics, such as medical instrumentation, sensors, wireless data acquisition, optogenetic instrumentation, and automated test systems development.



Helder Eiki Oshiro received the B.S. degree in electrical engineering from the Federal University of Sao Carlos (UFSCar), São Carlos, Brazil, in 2019. He is currently pursuing the M.S. degree in electrical engineering with the University of Sao Paulo (USP), São Carlos. Since 2017, he has been working with the Engineering Team, Braincare Desenvolvimento e Inovação Tecnológica S.A.



Caio Kioshi Miyazaki received the B.S. degree in electrical engineering from the University of Sao Paulo, São Carlos, Brazil, in 2017, where he is currently pursuing the M.S. degree in electrical engineering. He is working in product development at Braincare Desenvolvimento e Inovação Tecnológica S.A.



Cintya Yukie Hayashi received the B.S. degree in nursing from the School of Nursing, University of Sao Paulo, São Paulo, Brazil, in 2011, the Cardiology Nurse Specialist degree from the Heart Institute of Hospital das Clínicas da Faculdade de Medicina da USP, University of Sao Paulo in 2013, and the M.S. degree in neurosciences from the Faculty of Medicine, University of Sao Paulo in 2018, where she is currently pursuing the Ph.D. degree in neurosciences. From 2012 to 2013, she worked as a Registered Nurse with the Emergency Department, University of Sao Paulo Hospital. From 2013 to 2015, she was the Course Coordinator of the Brazilian Committee on Trauma for Advanced Trauma Life Support Program in Brazil and Latin America (region XIV), in partnership with the American College of Surgeons. She is a Clinical Research Nurse Coordinator at Braincare Desenvolvimento e Inovação Tecnológica S.A., Brazil. She participated in the International Junior Year Abroad Programme (Adult Nursing) at the School of Healthcare, University of Leeds, Leeds, U.K., in 2009.



Marcos Antonio de Morais received the degree in system analysis and development from the Federal Institute of Sao Paulo-IFSP, São Carlos, Brazil, in 2012. He has experience in the development of automation systems, supervised software, manufacturer control, design and assembly of electrical panels, and integration of equipment and instrumentation. He is responsible for development and implementation test procedures of products at Braincare Desenvolvimento e Inovação Tecnológica S.A.



Rodrigo Brunelli received the B.S. degree in computational physics from the University of Sao Paulo, São Carlos, Brazil, in 2013. He currently works as a Quality Assurance Manager and the Leader in firmware developer embedded systems at Braincare Desenvolvimento e Inovação Tecnológica S.A. He has experience with medical devices and embedded systems, working on the following topics, such as medical instrumentation, sensors, serial and wireless communications, and software quality.



João Paulo Carmo received the Ph.D. degree in industrial electronics. He is a Professor with the University of Sao Paulo (USP), São Carlos, Brazil. He is involved in research on micro/nanotechnologies, solid-state integrated sensors, and microdevices for biomedical and industrial applications. He is the Vice-Director of the Group of Metamaterials, Microwaves, and Optics (GMeta).